Joint inversion of gravity and traveltime data using a level-set based structural parametrization

Wenbin Li[1] **and Jianliang Qian**[2]

[1] *Department of Mathematics, Michigan State University, East Lansing, MI 48824. Email:* **wenbinli@math.msu.edu**

[2] *Department of Mathematics, Michigan State University, East Lansing, MI 48824. Email:* **qian@math.msu.edu**

(May 20, 2016)

Running head: **Level-set inversion of gravity and traveltime**

ABSTRACT

We propose a new level-set based structural parametrization for joint inversion of gravity and traveltime data so that density contrast and seismic slowness are simultaneously recovered in the inverse problem. Since density contrast and slowness are different model parameters of the same survey domain, we assume that they are similar in structure in terms of how each property changes and where the interface is located so that we are able to use a level-set function to parameterize the common interface shared by these two model parameters. The level-set parametrization makes it easy to maintain the structural similarity between the two geophysical properties. The inversion of gravity and traveltime data is carried out by minimizing a joint data-fitting function with respect to density contrast, slowness as well as the level-set function. An adjoint state method is used to compute the traveltime gradient efficiently. We test our algorithm on various synthetic examples, including a 2-D ovoid model and the 2-D SEG/EAGE salt model. The results show that the joint-inversion algorithm effectively improves recovery of subsurface features. To the best of our knowledge, this is the first time that the level-set method is used to structurally link density contrast and slowness distribution systematically.

INTRODUCTION

Geoscientists are well aware of the ambiguity in geophysical/geological interpretation, particularly in the case of potential field data (Krieger and Geisler, 2009). As exploration for minerals or hydrocarbon resources moves to increasingly complex geological environments, the integration of multiple physical measurements is needed to build improved earth models (Tartaras et al., 2011). Since joint inversion of gravity data and seismic traveltimes is a strategy that allows integration of different geophysical data sets at the inversion level, we propose a level-set based structural parametrization approach for joint inversion of gravity and traveltime data.

Interpretation of traveltime data can yield estimates of seismic slowness and layer geometry, provided that the survey region is well illuminated by rays between borehole and borehole or between borehole and surface. The low-resolution problem can arise in seismic interpretation when there are complex geological structures such as overthrust strata, volcanic layers, buried reefs and salt domes (Bain et al., 1991; Eaton et al., 2003), and it is exactly in these complex geological environments where the gravity field often has its greatest expression since gravity data show visible anomalies in regions with density contrasts. Moreover, as pointed out in Lelièvre et al. (2012), the surface gravity data provide high lateral resolution but poor depth resolution, and borehole-borehole or surface-borehole seismic traveltimes may provide high vertical resolution but poor lateral resolution. Therefore joint inversion of gravity data and seismic traveltimes is a natural consideration to reduce ambiguity of interpretation and improve reconstruction of subsurface features.

Since density contrast generates gravity anomalies and slowness affects formation of seismic traveltimes, it is essential to establish relationship between these two different properties so that gravity data and traveltime data can complement each other in interpretations. An explicit approach, when applicable, is to specify a simple analytic formula between the values of density and slowness (Birch, 1961; Gardner et al., 1974; Savino et al., 1982; Nielsen and Jacobsen, 2000; Afnimar et al., 2002). For instance, Nielsen and Jacobsen (2000) apply a linear relation with $S^{-1} = b\rho + a$ and Afnimar et al. (2002) derive a log-linear formula with $\rho = a \ln S + b$, where ρ denotes density, S

denotes slowness, and a and b are empirical parameters with different values in different formulas. These explicit relations reduce the two geophysical properties to one feature so that there is only one single model to recover in joint inversion. Following Lelièvre et al. (2012), we call such approach the compositional approach, since the analytic formula relating density and slowness relies on the geological composition of the surveyed domain. The density-slowness relations are different in different minerals. The analytic density-slowness formulas are sometimes applicable to sedimentary rocks but rarely to metamorphic rocks. Moreover, geological environment also has effects on compositional relations in that both temperature and pressure can affect the density-slowness formulas (Nielsen and Jacobsen, 2000). In practice, a high degree of uncertainty in analytic formulas is a major drawback of the compositional approach in joint inversion.

A less restrictive approach to joint inversion is to assume structural similarity between different causative geophysical properties (Haber and Oldenburg, 1997; Moorkamp et al., 2011; Gallardo-Delgado et al., 2003; Hering et al., 1995). Instead of applying a compositional formula, the structural approach assumes that the causative model parameters share a common structure in the spatial distribution so that different geophysical properties are similar in terms of how each property changes spatially and where the interface or boundary is located.

A widely used structural approach is the cross-gradient method (Gallardo and Meju, 2004, 2007; Linde et al., 2008; Fregoso and Gallardo, 2009; De Stefano et al., 2011), where the cross-product of gradients is used to measure similarity in structure between different model parameters. The idea is that if two parameters are similar in the spatial distribution their gradient vectors should be aligned so that the cross-product goes to zero. The cross-gradient norm is incorporated into the objective function and minimized in joint-inversion algorithms. A similar approach, yet different from the cross-gradient method, is the curvature method. Haber and Oldenburg (1997) develop a measure of structural similarity based on curvatures of model parameters, where the structural similarity between model parameters is indicated by a carefully chosen curvature operator. Both methods can be viewed as a non-parametric structural approach. The similarity in structure is enforced by minimizing a penalty function, and there is no explicit parametrization to specify the

common structure of model parameters. The flexible nature of the non-parametric approach makes them widely applicable, but improvement in the inversion results varies due to the loose constraint of structural similarity Lelièvre et al. (2012).

Some structure-parameterization methods for joint inversion enforce shared interface or boundary parametrization between model parameters. For example Hering et al. (1995) divide the subsurface into layers so that multiple geophysical properties are assumed to share the same interface between layers; Gallardo-Delgado et al. (2003) assemble a set of vertical prisms to accommodate the common structure of model parameters. One can refer to Lelièvre et al. (2015) for more methods using structural parameterization. The parametric methods enhance the structure of interface or boundary shared by causative geophysical properties so that they yield more apparent improvement in joint inversion than the non-parametric approaches do. However, the assumed simple geometry such as layers or vertical prisms hinders its application to complicated geological structures so that a non-generic parametrization can only be applied to specific earth scenarios.

To develop a generic structural parameterization, we propose to apply the level-set parametrization method (Osher and Sethian, 1988; Osher and Santosa, 2001) so as to accommodate the structural relation between causative geophysical properties. Both density contrast and seismic slowness are parameterized by the same level-set function so that the common interfaces identified by the zero level-set are enhanced by joint inversion. To the best of our knowledge, this is the first time that the level-set method is used to systematically link density contrast and slowness in a structurally coherent way.

The level-set method has been widely used in analysis of interfaces and shapes due to its ability in handling connectivity changes automatically. Complicated structures including disjoint components in geometry can be manipulated by the level-set parametrization. The level-set method was first used for inverse obstacle problems in Santosa (1996), and it has then been applied to a variety of inverse problems; see Litman et al. (1998); Osher and Santosa (2001); Hou et al. (2004); van den Doel et al. (2010); Papadopoulos et al. (2011); Zheglova et al. (2013); Lu and Qian (2015);

Li et al. (2015), and the references therein. Isakov et al. (2011) first apply the level-set method to the gravity data. Based on some uniqueness theorems, the level-set function is applied to parameterize some homogeneous source bodies. Li et al. (2016) applied the level-set method to image salt structures using gravity data. The level-set method also found its applications in seismic traveltime tomography. In Li and Leung (2013) a level-set-based adjoint state method is developed for inversion of first-arrival transmission traveltimes. This approach is further applied to inversion of cross-well transmission-reflection traveltimes in Li et al. (2014). So far no level-set method has been developed for joint inversion of traveltime and gravity data. Since the level-set function can naturally accommodate the common structure shared by different geophysical parameters, we develop a level-set-based structural parametrization to exploit the hidden relation of gravity and traveltime data so that joint inversion of gravity data and seismic data can be carried out effectively.

The rest of this paper is organized as follows. At first we present the model setup of the joint inverse problem. Then we develop the level-set parametrization for joint inversion of gravity data and seismic traveltimes. Following that, we summarize the algorithm and discuss some implementation details. We show various synthetic examples to demonstrate the effectiveness of our algorithm, where we mainly work on a 2-D ovoid model and the 2-D SEG/EAGE salt model. Finally, we draw our conclusion.

THE JOINT INVERSE PROBLEM

We use gravity data and first-arrival traveltimes simultaneously to invert for the density-contrast structure and slowness distribution of the same earth region. The gravity data is the anomalous acceleration generated by a mineral deposit or oil reservoir:

$$g_z(\tilde{\mathbf{r}}) = \gamma \int_\Omega K_z(\tilde{\mathbf{r}}, \mathbf{r}) \cdot \rho(\mathbf{r})\, \mathrm{d}\mathbf{r}, \qquad \tilde{\mathbf{r}} \in \Gamma_g, \tag{1}$$

where Ω denotes the survey domain, $\mathbf{r} = (x, z)$ is the spatial coordinate, $\rho(\mathbf{r})$ is the density contrast between the anomalous mass and the background, the universal gravitational constant

$\gamma \equiv 6.67384 \times 10^{-8}\text{cm}^3\text{g}^{-1}\text{s}^{-2}$, Γ_g is the measurement surface with $\tilde{\mathbf{r}}$ denoting the location of gravimeters, and the integration factor $K_z(\tilde{\mathbf{r}}, \mathbf{r})$ is the gravity kernel,

$$K_z(\tilde{\mathbf{r}}, \mathbf{r}) = -\frac{\tilde{z} - z}{|\tilde{\mathbf{r}} - \mathbf{r}|^n}, \tag{2}$$

with $n = 3$ in the 3-D space and $n = 2$ in the 2-D space. We assume that the gravity data are collected on a surface slightly above the survey domain.

On the other hand, seismic traveltimes are modeled by the eikonal equation:

$$|\nabla T(\mathbf{r})| = S(\mathbf{r}), \qquad \mathbf{r} \in \Omega \setminus \{\mathbf{r_s}\}, \tag{3a}$$

$$T(\mathbf{r_s}) = 0, \qquad \mathbf{r_s} \in P, \tag{3b}$$

where $T(\mathbf{r})$ is the traveltime from the point source $\mathbf{r_s}$ to $\mathbf{r}$, and P denotes the set of point sources; $S(\mathbf{r})$ is the slowness distribution. The traveltime data are collected on a part of the boundary of the survey domain, and we denote the measurement line to be $\Gamma_t \subset \partial\Omega$. We use the fast sweeping method (Zhao, 2005) to compute the viscosity solution of the eikonal equation, which corresponds to the first-arrival traveltime used in the inverse problem.

The joint inverse problem is stated as the following: given gravity acceleration data g_z on Γ_g and first-arrival traveltimes T on Γ_t, one inverts for the density contrast ρ and the slowness distribution S simultaneously in Ω. Figure 1 displays an example of the problem setup.

JOINT INVERSION USING THE LEVEL-SET METHOD

Structural relation and a level-set parametrization

The effectiveness of the joint inversion relies on the physical relation between density contrast ρ and slowness distribution S. Since ρ and S are different model parameters of the same survey domain, we assume that they share a common structure in the spatial distribution. Since the two physical

properties are similar in terms of how each property changes spatially and where the interface is located, we propose a level-set formulation to parameterize the common structure shared by ρ and S.

Denoting the region occupied by the mineral by Ω_0 ($\Omega_0 \subset \Omega$), we define the level-set function

$$\phi(\mathbf{r}) = \begin{cases} > 0 & \mathbf{r} \in \Omega_0^{\text{int}}, \\ = 0 & \mathbf{r} \in \partial\Omega_0, \\ < 0 & \mathbf{r} \in \Omega \setminus \overline{\Omega}_0, \end{cases} \tag{4}$$

where Ω_0^{int}, $\overline{\Omega}_0$ and $\partial\Omega_0$ are interior, closure and boundary of region Ω_0, respectively. Since the two model-parameters ρ and S have the same interfaces in the survey domain, the zero level-set of ϕ indicates the interfaces which separate the mineral from its sedimentary background. Consequently, the density contrast ρ is expressed as

$$\rho(\mathbf{r}) = \rho_0(\mathbf{r}) \cdot H(\phi(\mathbf{r})) \tag{5}$$

and the slowness distribution $S(\mathbf{r})$ is given by

$$S(\mathbf{r}) = S_1(\mathbf{r}) \cdot H(\phi(\mathbf{r})) + S_2(\mathbf{r}) \cdot (1 - H(\phi(\mathbf{r}))), \tag{6}$$

where ρ_0, S_1, and S_2 are functions to be determined. In equations (5) and (6) $H(\phi)$ is the Heaviside function with

$$H(\phi) = \begin{cases} 1 & , \quad \phi > 0 \\ 0.5 & , \quad \phi = 0 \\ 0 & , \quad \phi < 0 \end{cases} . \tag{7}$$

By definition of the level-set function $\phi(\mathbf{r})$ and the Heaviside function $H(\phi)$ one can find that

$$\rho(\mathbf{r}) = \begin{cases} \rho_0(\mathbf{r}) & , \quad \mathbf{r} \in \Omega_0^{\text{int}} \\ 0 & , \quad \mathbf{r} \in \Omega \setminus \overline{\Omega}_0 \end{cases} \quad \text{and} \quad \mathrm{S}(\mathbf{r}) = \begin{cases} S_1(\mathbf{r}) & , \quad \mathbf{r} \in \Omega_0^{\text{int}} \\ S_2(\mathbf{r}) & , \quad \mathbf{r} \in \Omega \setminus \overline{\Omega}_0 \end{cases} ; \tag{8}$$

here ρ_0 is the density contrast; S_1 is the inner-region slowness and S_2 is the outer-region slowness. Since the level-set function ϕ is the common parameter in representations of the density contrast ρ and the slowness distribution S, it captures the structural relation between the two different physical properties.

Data fitting and optimization

The data misfit of gravity acceleration is measured by

$$E_g = \frac{1}{2}\int_{\Gamma_g} (g_z - g_z^*)^2 \, \mathrm{d}\tilde{\mathbf{r}}, \tag{9}$$

where g_z^* denotes the observed gravity acceleration on Γ_g, and g_z is the predicted gravity acceleration from the forward model in equation (1). Similarly, the traveltime misfit is measured by

$$E_t = \frac{1}{2}\sum_j \int_{\Gamma_t} \left(T_j - T_j^*\right)^2 \, \mathrm{d}s; \tag{10}$$

T_j^* denotes first-arrival traveltime induced by the point source located at $\mathbf{r}_\mathbf{s}^j$, and T_j is the viscosity solution of the eikonal equation (3a) with the point-source boundary condition (3b) at $\mathbf{r}_\mathbf{s}^j$; j is the index of point sources, and Γ_t denotes the measurement surface in seismic survey. Although we do not include the information of data uncertainties in equations (9) and (10), one can simply include such information in the misfit functions.

The joint misfit function is proposed as a linear combination of E_g and E_t:

$$E_J = w \cdot E_g + E_t, \tag{11}$$

where the weight parameter w balances the contributions of the two data-misfit terms. The choice of w will be specified in the section of *summary of algorithm* and the section of *numerical examples*.

The geological structure of the survey domain is parameterized by ϕ, ρ_0, S_1 and S_2 in equations

(5) and (6). We invert for these parameters by minimizing the joint misfit function proposed in equation (11). Since density contrast is directly related to gravity and slowness is directly related to traveltime, it is straightforward to obtain the following formulas:

$$\frac{\partial E_J}{\partial \rho_0} = w \cdot \frac{\partial E_g}{\partial \rho_0}\,; \tag{12a}$$

$$\frac{\partial E_J}{\partial S_i} = \frac{\partial E_t}{\partial S_i}\,, \qquad i = 1, 2\,; \tag{12b}$$

$$\frac{\partial E_J}{\partial \phi} = w \cdot \frac{\partial E_g}{\partial \phi} + \frac{\partial E_t}{\partial \phi}\,. \tag{12c}$$

Therefore, the gradient direction of the joint misfit function can be evaluated according to those of E_g and E_t. Essentially the gradient direction of E_g can be computed directly since the density contrast and the gravity data are explicitly related through an integral equation; the gradient of E_t is evaluated by an adjoint state method. The detailed analysis and derivations can be found in Isakov et al. (2011); Li et al. (2016); Leung and Qian (2006); Li and Leung (2013); Li et al. (2014).

The gradient direction of E_g can be evaluated directly with

$$\frac{\partial E_g}{\partial \phi}(\mathbf{r}) = \rho_0 \cdot \delta_d(\phi) \cdot \gamma \int_{\Gamma_g} (g_z(\tilde{\mathbf{r}}) - g_z^*(\tilde{\mathbf{r}})) \cdot K_z(\tilde{\mathbf{r}}, \mathbf{r})\, \mathrm{d}\tilde{\mathbf{r}}\,, \tag{13a}$$

$$\frac{\partial E_g}{\partial \rho_0}(\mathbf{r}) = H(\phi) \cdot \gamma \int_{\Gamma_g} (g_z(\tilde{\mathbf{r}}) - g_z^*(\tilde{\mathbf{r}})) \cdot K_z(\tilde{\mathbf{r}}, \mathbf{r})\, \mathrm{d}\tilde{\mathbf{r}}\,, \tag{13b}$$

where $H(\phi)$ is the Heaviside function and $\delta_d(\phi)$ is the Dirac delta function. In some specific applications the density contrast ρ_0 can be assumed to be constant, and the corresponding derivative is evaluated by

$$\frac{\partial E_g}{\partial \rho_0} = \frac{1}{|\Omega|} \cdot \int_\Omega \left[H(\phi) \cdot \gamma \int_{\Gamma_g} (g_z(\tilde{\mathbf{r}}) - g_z^*(\tilde{\mathbf{r}})) \cdot K_z(\tilde{\mathbf{r}}, \mathbf{r})\, \mathrm{d}\tilde{\mathbf{r}} \right] \mathrm{d}\mathbf{r}\,, \tag{13b'}$$

where $|\Omega|$ denotes the measure (area or volume) of the domain Ω. The formula (13b') is the average value of (13b) in the survey domain.

The gradient direction of E_t is evaluated by the adjoint state method (Leung and Qian, 2006).

For each set of traveltimes, an adjoint variable λ_j is introduced by solving the following equations:

$$-\nabla \cdot (\lambda_j \nabla T_j) = 0 \quad , \quad \text{in } \Omega \tag{14a}$$

$$\lambda_j \cdot \frac{\partial T_j}{\partial \mathbf{n}} = T_j - T_j^* \quad , \quad \text{on } \Gamma_t \tag{14b}$$

$$\lambda_j = 0 \quad , \quad \text{on } \partial\Omega \setminus \Gamma_t \tag{14c}$$

where $\mathbf{n}$ denotes the outer unit normal of the boundary. This adjoint-state equation can be solved by the fast sweeping method proposed in Leung and Qian (2006). Accordingly, the gradient of E_t is evaluated by the following formulas:

$$\frac{\partial E_t}{\partial \phi}(\mathbf{r}) = \left(\sum_j \lambda_j(\mathbf{r}) \right) \cdot S(\mathbf{r}) \cdot (S_1(\mathbf{r}) - S_2(\mathbf{r})) \cdot \delta_d(\phi(\mathbf{r})), \tag{15a}$$

$$\frac{\partial E_t}{\partial S_1}(\mathbf{r}) = \left(\sum_j \lambda_j(\mathbf{r}) \right) \cdot S(\mathbf{r}) \cdot H(\phi(\mathbf{r})), \tag{15b}$$

$$\frac{\partial E_t}{\partial S_2}(\mathbf{r}) = \left(\sum_j \lambda_j(\mathbf{r}) \right) \cdot S(\mathbf{r}) \cdot (1 - H(\phi(\mathbf{r}))) \ . \tag{15c}$$

Substituting formulas (13a) and (15a) into equation (12c) yields

$$\frac{\partial E_J}{\partial \phi} = \left[w \cdot \rho_0 \cdot \gamma \int_{\Gamma_g} (g_z(\tilde{\mathbf{r}}) - g_z^*(\tilde{\mathbf{r}})) \cdot K_z(\tilde{\mathbf{r}}, \mathbf{r}) \, \mathrm{d}\tilde{\mathbf{r}} + \left(\sum_j \lambda_j(\mathbf{r}) \right) \cdot S(\mathbf{r}) \cdot (S_1(\mathbf{r}) - S_2(\mathbf{r})) \right] \cdot \delta_d(\phi(\mathbf{r})). \tag{16}$$

From equation (12a), $\frac{\partial E_J}{\partial \rho_0}$ is evaluated by multiplying the weight parameter w to $\frac{\partial E_g}{\partial \rho_0}$ which is given by equation (13b) or equation (13b'). According to equation (12b) $\frac{\partial E_J}{\partial S_i}$ is equal to $\frac{\partial E_t}{\partial S_i}$ $(i = 1, 2)$.

In summary, we have computed the gradient direction of the joint misfit function E_J so that we can use the method of gradient descent to evaluate a minimizer. The model parameters ϕ, ρ_0,

S_1 and S_2 are updated iteratively along the negative gradient direction:

$$(-\frac{\partial E_J}{\partial \phi}, -\frac{\partial E_J}{\partial \rho_0}, -\frac{\partial E_J}{\partial S_1}, -\frac{\partial E_J}{\partial S_2}).$$

The iteration is considered to be convergent when there is no further reduction in the misfit function. If there is a priori knowledge of some model parameters, our algorithm has the flexibility to use such a priori information as we can fix those parameters during iterations.

Regularization

We adopt the reinitialization technique to regularize the level-set function $\phi(\mathbf{r})$. The idea is to reinitialize ϕ to be a signed-distance function to the interface, since the signed-distance function smoothens ϕ without moving the zero level-set which parameterizes the shape of interface. Mathematically, it can be achieved by solving the following equation in an artificial time direction ξ up to a steady state,

$$\frac{\partial \Phi}{\partial \xi} + \text{sign}(\phi) \cdot (|\nabla \Phi| - 1) = 0\,, \tag{17a}$$

$$\left.\frac{\partial \Phi}{\partial \mathbf{n}}\right|_{\partial\Omega} = 0\,, \tag{17b}$$

where the initial condition $\Phi|_{\xi=0} = \phi$ and $\text{sign}(\phi)$ is the signum function which extracts the sign of a real number (Sussman et al., 1994). This equation can be solved by some upwinding schemes (Qian and Symes, 2002; Cecil et al., 2006). In practice, however, since we are interested in the solution only near the zero level-set, we simply solve the equation for several $\Delta\xi$ steps (in our numerical example only one step) and the intermediate solution Φ is used to replace the original level-set function. Other regularization procedures might also be used rather than the one we are proposing here. For example, one might also try to regularize the length of boundaries by including the total variation of ϕ in the energy functional (Rudin et al., 1992). In this work, however, we do not explore this possibility.

As for the density contrast ρ_0 and the slowness distributions S_i $(i = 1, 2)$, we regularize their corresponding perturbations $\frac{\partial E_J}{\partial \rho_0}$, $\frac{\partial E_J}{\partial S_1}$, and $\frac{\partial E_J}{\partial S_2}$ at each iteration. To make a concise description of this methodology we denote q to be one of these model parameters. The corresponding gradient direction is $\frac{\partial E_J}{\partial q}(\mathbf{r})$ and the iteration of q is

$$q^{\text{new}}(\mathbf{r}) = q^{\text{old}}(\mathbf{r}) + \epsilon \cdot \tilde{q}(\mathbf{r}), \tag{18}$$

where $\tilde{q}(\mathbf{r}) = -\frac{\partial E_J}{\partial q}(\mathbf{r})$ and ϵ is the step size of iteration. We regularize the perturbation parameter $\tilde{q}(\mathbf{r})$ by solving the following equation:

$$(I - \alpha\Delta)\,\tilde{q}^* = \tilde{q}\,, \tag{19a}$$

$$\left.\frac{\partial \tilde{q}^*}{\partial \mathbf{n}}\right|_{\partial\Omega} = 0\,, \tag{19b}$$

where I is the identity operator, Δ is the Laplace operator, and $\alpha > 0$ is the weight controlling the amount of regularity that one wants; in our numerical experiments we set $\alpha = 1$. Then $\tilde{q}^*$ is used to replace $\tilde{q}$ during iteration. One can show that $\tilde{q}^*$ is still a descent direction which reduces the misfit function:

$$\begin{aligned} E(q + \epsilon \cdot \tilde{q}^*) - E(q) &\doteq \epsilon \cdot \int_\Omega \frac{\partial E}{\partial q}(\mathbf{r}) \cdot \tilde{q}^*(\mathbf{r})\,\mathrm{d}\mathbf{r} \\ &= -\epsilon \cdot \int_\Omega \tilde{q}(\mathbf{r}) \cdot \tilde{q}^*(\mathbf{r})\,\mathrm{d}\mathbf{r} \\ &= -\epsilon \cdot \int_\Omega (I - \alpha\Delta)\tilde{q}^* \cdot \tilde{q}^*\,\mathrm{d}\mathbf{r} \\ &= -\epsilon \cdot \int_\Omega \left[(\tilde{q}^*)^2 + \alpha|\nabla \tilde{q}^*|^2\right]\,\mathrm{d}\mathbf{r} \le 0. \end{aligned} \tag{20}$$

See Leung and Qian (2006) for more details on such regularization.

SUMMARY OF ALGORITHM

We summarize the joint-inversion algorithm.

Algorithm

1. Initialize the level-set function ϕ, density contrast ρ_0, and slowness distributions S_1 and S_2.
2. Construct $\rho(\mathbf{r})$ and $S(\mathbf{r})$ by equation (5) and equation (6).
3. Compute the gravity acceleration $g_z(\tilde{\mathbf{r}})$ according to equation (1); obtain the first-arrival traveltime T_j by solving the eikonal equations (3a) and (3b) for each point source $\mathbf{r}_{\mathbf{s}}^j$.
4. Obtain the adjoint variable λ_j by solving the adjoint-state equations (14a)-(14c) for each j.
5. Compute the gradient direction $(\frac{\partial E_J}{\partial \phi}, \frac{\partial E_J}{\partial \rho_0}, \frac{\partial E_J}{\partial S_1}, \frac{\partial E_J}{\partial S_2})$ and take $(\tilde{\phi}, \tilde{\rho_0}, \tilde{S_1}, \tilde{S_2}) = (-\frac{\partial E_J}{\partial \phi}, -\frac{\partial E_J}{\partial \rho_0}, -\frac{\partial E_J}{\partial S_1}, -\frac{\partial E_J}{\partial S_2})$.
6. Regularize the perturbation parameters $\tilde{\rho_0}$, $\tilde{S_1}$ and $\tilde{S_2}$ by solving equations (19a)-(19b) for each $\tilde{q} \in \{\tilde{\rho_0}, \tilde{S_1}, \tilde{S_2}\}$.
7. Update the model parameters with $\phi^{\text{new}} = \phi^{\text{old}} + \epsilon \cdot \tilde{\phi}$, $\rho_0^{\text{new}} = \rho_0^{\text{old}} + \epsilon \cdot \tilde{\rho}_0^*$, $S_1^{\text{new}} = S_1^{\text{old}} + \epsilon \cdot \tilde{S}_1^*$, $S_2^{\text{new}} = S_2^{\text{old}} + \epsilon \cdot \tilde{S}_2^*$, where ϵ is the step size of iteration.
8. Reinitialize the level-set function ϕ by solving (17a)-(17b), and use Φ to update ϕ.
9. Go back to step 2 until the iteration converges.

In step 1, the level set function ϕ is initialized to be a signed distance function to an initial guess of the interface; ρ_0, S_1 and S_2 can be initialized to be any reasonable values. We will illustrate the setup of initialization in numerical examples.

The Heaviside function $H(\phi)$ is numerically approximated by

$$H_\tau(\phi) = \begin{cases} 0 & , \quad \phi < -\tau \\ \frac{1}{2} + \frac{\phi}{2\tau} + \frac{1}{2\pi}\sin\left(\frac{\pi\phi}{\tau}\right) & , \quad -\tau \le \phi \le \tau \\ 1 & , \quad \tau < \phi \end{cases} \tag{21}$$

where τ is a small parameter controlling the interface thickness, and we set $\tau = 0.5\min\{\Delta x, \Delta z\}$ in the computation.

In step 5, $\tilde{\phi} = -\frac{\partial E_J}{\partial \phi}$ is evaluated from equation (16), where the Dirac delta function $\delta_d(\phi)$ is numerically evaluated by $(\delta_d)_\tau(\phi) = \mathcal{I}_{T_\tau} \cdot |\nabla\phi|$ (Zhao et al. (1996); Lu et al. (2015); Lu and Qian (2015); Li et al. (2015)); here T_τ denotes the set $\{\mathbf{r} \in \Omega : \ |\phi(\mathbf{r})| \le \tau\}$ and $\mathcal{I}_{T_\tau}$ is the characteristic function with

$$\mathcal{I}_{T_\tau}(\mathbf{r}) = \begin{cases} 1 & , \quad \mathbf{r} \in T_\tau \\ 0 & , \quad \mathbf{r} \in \Omega \setminus T_\tau \end{cases} . \tag{22}$$

In computation, the parameter $\tau = 0.5\min\{\Delta x, \Delta z\}$.

Substituting the numerical delta function into equation (16) one gets

$$\tilde{\phi} = -V \cdot |\nabla\phi|, \tag{23}$$

where

$$\begin{aligned} V \ = \ & \mathcal{I}_{T_\tau}(\mathbf{r}) \cdot \Bigg[w \cdot \rho_0 \cdot \gamma \int_{\Gamma_g} (g_z(\tilde{\mathbf{r}}) - g_z^*(\tilde{\mathbf{r}})) \cdot K_z(\tilde{\mathbf{r}}, \mathbf{r}) \, \mathrm{d}\tilde{\mathbf{r}} \\ & + \left(\sum_j \lambda_j(\mathbf{r}) \right) \cdot S(\mathbf{r}) \cdot (S_1(\mathbf{r}) - S_2(\mathbf{r})) \Bigg] . \end{aligned} \tag{24}$$

Then in step 7 the level-set function is updated by

$$\phi^{\text{new}} = \phi^{\text{old}} - \epsilon \cdot V \cdot |\nabla\phi| \,, \tag{25}$$

where the step size ϵ is chosen to satisfy the Courant-Friedrichs-Lewy (CFL) stability condition,

$$\epsilon \cdot \left(\frac{\max |V|}{\min\{\Delta x, \Delta z\}} \right) < 1. \tag{26}$$

In practice we take the step size to be

$$\epsilon = \min \left\{ c_1 \, , \, c_2 \frac{\min\{\Delta x, \Delta z\}}{\max |V|} \right\}, \tag{27}$$

where c_2 is a CFL constant which is taken to be 0.5 in our computations, and c_1 is a small positive number which aims to further control the updating step size during iteration.

The principle of choosing the weight parameter w is to make the two data sets have comparable effects in the joint inversion. Since the level-set function ϕ is updated in the direction of $-\frac{\partial E_J}{\partial \phi}$ with $\frac{\partial E_J}{\partial \phi} = w \cdot \frac{\partial E_g}{\partial \phi} + \frac{\partial E_t}{\partial \phi}$, one can set

$$w = \frac{\max \left| \frac{\partial E_t}{\partial \phi} \right|}{\max \left| \frac{\partial E_g}{\partial \phi} \right|} \tag{28}$$

or

$$w = \frac{\text{average} \left| \frac{\partial E_t}{\partial \phi} \right|}{\text{average} \left| \frac{\partial E_g}{\partial \phi} \right|}, \tag{29}$$

such that E_g and E_t have comparable contributions to the updating of ϕ. This strategy requires re-computing w in each iteration so that the value of w changes at each step. If we have good knowledge of the respective weight of the gravity data and the traveltime data, w can be simply fixed to be an appropriate constant.

NUMERICAL EXAMPLES

We demonstrate the performance of the joint-inversion algorithm in three different scenarios: (1) given a priori density contrast and slowness, we are going to recover shape only, which leads to a

shape recovery problem; (2) given a priori density contrast and partial information on slowness, we are going to recover both shape and slowness, which leads to a shape-slowness recovery problem; and (3) given partial information on slowness, we are going to recover shape, slowness and density contrast simultaneously.

Shape recovery

This shape-recovery example demonstrates the effect of joint inversion, where the density parameter ρ_0 in formula (5) and the inner-region slowness S_1 and the outer-region slowness S_2 in formula (6) are assumed to be known. We only invert for the level-set function ϕ, which appears in both representations of the anomalous density contrast ρ and the slowness distribution S.

We consider a 2-D slice of the SEG/EAGE salt model proposed in Aminsadeh (1996). The original SEG/EAGE salt model is a velocity model designed to challenge contemporary seismic imaging methods. To test our algorithm for joint inversion, we have captured the structure of the salt body, and accordingly we have constructed the following density-slowness model. The profile of the 2-D salt body is shown in Figure 2, where Figure 2 (a) shows the density model and Figure 2 (b) shows the slowness model. The value of the density contrast is set to be $\rho_0(\mathbf{r}) = 0.2\ \mathrm{g}\cdot\mathrm{cm}^{-3}$; the outer-region slowness is $S_2(\mathbf{r}) = 0.5\,\mathrm{s/km}$ and the inner-region slowness is taken as $S_1(x,z) = \left(0.2 - \frac{z-2100}{15000}\right)$ s/km, which simulates a linearly decreasing slowness with respect to depth. We use this example to illustrate the effect of the joint-inversion algorithm when no explicit compositional relation is assumed for density and slowness.

The computational domain is $\Omega = [0, 13400]\,\mathrm{m} \times [0, 4000]\,\mathrm{m}$, which is uniformly discretized into 68×21 mesh grids. To perform the inversion algorithm, we initialize the level-set function to be the signed distance to an ellipse with the semi-major axis of 4000 m and the semi-minor axis of 1000 m; Figure 3 (a) displays the initial density and Figure 3 (b) shows the initial slowness. In the computation we use a numerical Heaviside function given by formula (21); therefore the numerical interface has a finite width, which is the reason of fuzziness in images near interfaces. We have

performed the gravity inversion, the traveltime inversion, and the joint inversion respectively so that we can compare the results.

Figure 4 (a) shows the recovered solution by the gravity inversion only, and Figure 4 (b) shows the recovered solution by the traveltime inversion only. The solid line plots the zero contour of the level set function, which depicts the location of interface in the recovered solution; the dashed line outlines the true interface of the salt structure. To quantitatively assess the performance of shape recovery, we count the number of mesh grids with correctly recovered lithology and denote it to be C. The values of C are listed in captions of the figures. In Figure 4 (c) and Figure 4 (d) we provide the convergence history of gravity inversion and traveltime inversion, respectively. In the gravity inversion, the misfit function descends quickly at the beginning, and then it slowly goes to the steady state after 2000 iterations. We perform 3000 iterations to make sure that the convergence is achieved, and the CPU time of 3000 iterations is about 1.57 seconds on an equivalent 2.5 GHz processor. In the traveltime inversion, the misfit function descends to the steady state after 200 iterations, and we perform 1000 iterations to make sure that the convergence is achieved. The CPU time of the traveltime inversion is about 32.2 seconds on an equivalent 2.5 GHz processor. In both inversions, the iteration step ϵ is given by formula (27) with $c_1 = 0.5$ and $c_2 = 0.5$.

We use formula (28) to compute the value of w in the misfit function E_J after every iteration so that E_g and E_t have comparable contributions to the updating of the level set function. Figure 5 (a) shows the solution with the solid line contouring the recovered interface and the dashed line contouring the true interface. Figure 5 (b) shows the evolution of the joint misfit function E_J, which illustrates the history of convergence. The misfit function descends to the steady state after 500 iterations. The CPU time required for this inversion is about 47.9 seconds on an equivalent 2.5 GHz processor.

Comparing the results shown in Figure 4 (a), (b) and Figure 5 (a), we conclude that the joint inversion algorithm effectively improves the shape recovery of the salt structure. The inversion using only one type of data, either gravity acceleration or seismic first-arrival traveltimes, leads to an

incomplete recovery with distortions in the shape and location of interface. As shown in Figure 4 (a) and Figure 4 (b), both the gravity inversion and the traveltime inversion have successfully captured the overall structure of the salt body, but both fail to recover the horizontal extension and the steeply dipping flank. However, the joint inversion utilizes two types of data, which are expected to complement each other in their interpretations. As shown in Figure 5 (a), the recovered interface matches well with the true interface. The top of the salt body is well imaged and the steeply dipping flank is successfully recovered; moreover, the thin layer of the salt body stretching to the right is successfully captured. We denote C to be the number of mesh grids with correct lithology in the recovered solution; the value of C equals 1403 in the joint inversion, which is improved from the value $C = 1303$ in the gravity inversion and the value $C = 1300$ in the traveltime inversion. Since the level-set parametrization accommodates the common structure shared by the gravity inversion and traveltime inversion, the joint-inversion algorithm provides better resolution for the salt body.

The choice of the weighting parameter w in the misfit function E_J is of practical importance in joint inversion, and we use this example to illustrate the effect of w in our level-set algorithm. We have performed joint inversions by choosing different values of w; Figure 6 (a)-(d) provide the recovered solutions with $w = 0.1,\ 1,\ 10,$ and 100, respectively. The solid line contours the recovered interface and the dashed line displays the exact structure; C is the number of mesh grids with correct lithology in the recovered solution. One can find that when $w = 1$ C takes the largest value among the four cases, and a good recovery of the salt body is achieved similar to that of Figure 5 (a). When w decreases to 0.1 the solution is distorted away from the true structure so that it resembles the solution of traveltime inversion as shown in Figure 4 (b). This is reasonable because decreasing w leads to the situation that the gravity data weigh less than the traveltime data in the joint inversion. On the other hand, increasing w leads to the situation that the gravity data weigh more than the traveltime data in the joint inversion, as shown in Figure 6 (c)-(d). These results show that our algorithm works well on this synthetic example with a wide range of values in the weighting parameter w.

Shape-slowness recovery

Assuming that the density contrast ρ_0 in formula (5) is known, we invert for the level-set function ϕ and the slowness parameters $S_i, (i = 1, 2)$ simultaneously. The a priori knowledge of ρ_0 may reduce ambiguity in the interpretation of gravity data (Krahenbuhl and Li, 2006).

A 2-D salt model with varying inner-region slowness

We consider a salt model which has a constant density contrast $\rho_0 = 0.2\ \mathrm{g} \cdot \mathrm{cm}^{-3}$, a constant outer-region slowness $S_2(\mathbf{r}) = 0.5\,\mathrm{s/km}$ and a varying inner-region slowness $S_1(x, z) = \left(0.2 - \frac{z-2100}{15000}\right)$ s/km, as shown in Figure 2 (a) and Figure 2 (b).

Assuming that the density contrast ρ_0 and the outer-region slowness S_2 are given a priori information, we invert for the inner-region slowness S_1 and the level set function ϕ simultaneously in the joint inversion.

The computational domain is $\Omega = [0, 13400]\,\mathrm{m} \times [0, 4000]\,\mathrm{m}$, which is uniformly discretized into 68×21 mesh grids. To perform the inversion algorithm, we initialize the level set function to be the signed distance to an ellipse with the semi-major axis of 4000 m and the semi-minor axis of 1000 m; the initial guess of the inner-region slowness is $S_1 = 0.3\,\mathrm{s/km}$. Figure 7 (a) shows the initial density contrast and Figure 7 (b) shows the initial slowness. Figure 7 (c) provides the recovered density contrast by the gravity inversion only; Figure 7 (d) provides the recovered slowness by the first-arrival traveltime inversion only. Both the gravity inversion and the traveltime inversion have good resolution in the shallow region of the salt body; however they fail to recover the steeply dipping flank in the deep region. In the joint inversion, we use formula (28) to compute the weight parameter w in the misfit function E_J. The iteration step ϵ is given by formula (27) with $c_1 = 0.1$ and $c_2 = 0.5$. The recovered density contrast is shown in Figure 7 (e) and the recovered slowness in Figure 7 (f), where the shape of the salt body is completely reconstructed and the dipping flank is successfully filled in by salt. Although the compositional relation between ρ_0 and S_1 is not

available, the varying property of the inner-region slowness is still well recovered.

To further test the robustness of algorithm we have repeated the joint inversion by contaminating the measurement data g_z^* and T^* with 2% Gaussian noise. The recovered density is shown in Figure 8 (a) and the recovered slowness is shown in Figure 8 (b). Since no apparent distortion in the recovered structure, the inversion is not sensitive to a small amount of Gaussian noise with zero mean.

A 2-D SEG/EAGE salt model

We consider a cross-section of the original SEG/EAGE salt model (Aminsadeh (1996)). As shown in Figure 9 (b), the slowness profile is taken from the SEG/EAGE salt model along a plane defined by three points: $A_1(0\text{m}, 2200\text{m}, 0\text{m})$, $A_2(13400\text{m}, 6600\text{m}, 0\text{m})$ and $A_3(13400\text{m}, 6600\text{m}, 4000\text{m})$. The salt body is an acoustically fast medium with the slowness $S_1 = (1/4.481)\,\text{s/km}$; the sedimentary background is acoustically slow with a varying distribution of slowness; moreover there is an anomaly of large-slowness deposit in the subsalt region. The density-contrast value is taken as $\rho_0(\mathbf{r}) = \frac{1800-z}{1000} \cdot 0.2\ \text{g} \cdot \text{cm}^{-3}$ and Figure 9 (a) shows the exact density profile. The density contrast between salt and its sediment is linearly decreasing with depth, which corresponds to the scenario with an increasing density in background and a relatively constant density in salt.

The gravity data g_z^* and the first-arrival traveltimes T^* are collected in the same way as the previous example. The computational domain $\Omega = [0, 13400]\,\text{m} \times [0, 4000]\,\text{m}$ is uniformly discretized into 68×21 mesh points. Assuming that the density contrast ρ_0 and inner-region slowness S_1 are given to be a priori information, we invert for the outer-region slowness S_2 and the level set function ϕ simultaneously in the joint inversion.

We initialize the level set function to be the signed distance to an ellipse with the semi-major axis of 4000 m and the semi-minor axis of 1000 m. The outer-region slowness is initialized to be $S_2 = 0.6\,\text{s/km}$. Figure 10 (a) shows the initial guess of density contrast and Figure 10 (b) shows the initial slowness. Figure 10 (c) shows the recovered density contrast by the gravity inversion

only, and Figure 10 (d) shows the recovered slowness by the traveltime inversion only. The crest of the salt body is successfully recovered in both density contrast and slowness; the dipping flank is partially imaged in the gravity inversion; the large-slowness structure in the subsalt region is not recovered in the traveltime inversion due to the distortion of the salt body in shape.

To perform the joint inversion we compute the weight parameter w by formula (28) and set the iteration step ϵ according to formula (27) with $c_1 = 0.03$ and $c_2 = 0.5$. The solution is shown in Figure 10 (e) and Figure 10 (f). The recovered density contrast and slowness share the same level-set function which parameterizes the shape of the salt body, and they are much improved in comparison to the results shown in Figure 10 (c) and Figure 10 (d). Although there is a slight distortion in the tip, the joint inversion has provided much better resolution in the steeply dipping flank. Due to the improvement of reconstruction the large-slowness structure beneath the salt sill is better perceived in the slowness profile, which provides useful information for the interpretation of the subsalt region.

To further test the robustness of the joint-inversion algorithm, we have contaminated the measurement data by 2% Gaussian noise with zero mean and repeated the joint-inversion process. The recovered density is shown in Figure 11 (a) and the recovered slowness is shown in Figure 11 (b), which are quite similar to the recovered solutions using clean measurements as shown in Figure 10 (e) and Figure 10 (f). These results, therefore, illustrate that the joint-inversion algorithm has the potential to handle realistic salt-imaging problems in the presence of reasonable noise contamination.

A 2-D ovoid model

In this example we consider a synthetic structure which is similar to the ovoid model used in Lelièvre et al. (2012). The exact structure is shown in Figure 12 (a) and 12 (b). The density contrast ρ_0 is set to be $\rho_0 = 2\ \mathrm{g} \cdot \mathrm{cm}^{-3}$, the inner-region slowness is $S_1 = 0.23$ s/km and the outer-region slowness is $S_2 = 0.16$ s/km. The ovoid body has larger slowness than its background, in which case the

first-arrival rays usually provide poor illumination in the inner region.

Taking the density contrast ρ_0 as a priori information, we invert for the level set function ϕ, the inner-region slowness S_1, and the outer-region slowness S_2 simultaneously in the joint inversion. This example aims to demonstrate that our algorithm is able to recover both shape and slowness without any specific knowledge in shape or slowness.

The computational domain is $\Omega = [-300, 400]\,\mathrm{m} \times [0, 200]\,\mathrm{m}$, which is uniformly discretized into 71×21 mesh points. To perform the inversion algorithm we initialize the ovoid body to be an ellipse with the semi-major axis of 300 m and the semi-minor axis of 70 m. Figure 13 (a) shows the initial density contrast and Figure 13 (b) shows the initial slowness. The initial guess of the inner-region slowness is set to be $S_1(\mathbf{r}) = 0.4$ s/km and the initial guess of the outer-region slowness is $S_2(\mathbf{r}) = 0.2$ s/km; we mention that these parameters are not constrained to be uniform in the inversion process. Figure 13 (c) shows the recovered density contrast by the gravity inversion only and Figure 13 (d) shows the recovered slowness by the first-arrival traveltime inversion only. As pointed out in Lelièvre et al. (2012), the gravity inversion provides better lateral resolution while the traveltime inversion leads to better depth resolution, which is consistent with our numerical results in this example.

In the joint inversion the weighting parameter w is computed according to formula (28). The iteration step ϵ is given by formula (27) with $c_1 = 0.2$ and $c_2 = 0.5$. Figure 13 (e) and Figure 13 (f) show the convergent solution of the joint inversion. Both lateral and depth locations of the two ovoid bodies are successfully recovered in the survey domain. The joint inversion has provided improved reconstruction. To display the slowness value more clearly we also provide the pictures of cross-sections in Figure 14; Figure 14 (a) shows the cross-section of the slowness along $x = 100$ m and Figure 14 (b) shows the slowness along $z = 100$ m. Comparing the recovered slowness with the exact slowness, we conclude that the outer region slowness $S_2(\mathbf{r}) = 0.2$ s/km is almost perfectly recovered but the inner-region slowness S_1 is not recovered well. This is mainly due to the poor illumination of the first-arrival rays, since in this example the ovoid body has

larger slowness than its background; we may have little information in the inner-region slowness if the rays corresponding to first-arrivals at the geophones do not penetrate the ovoid body. The recovery of S_1 can be improved by incorporating multi-arrival traveltimes into the tomography or by enforcing an explicit compositional relation between density contrast and slowness (Lelièvre et al., 2012). However, in this example the false value of S_1 has not significantly affected the shape recovery of the ovoid body, provided that the inner-region slowness S_1 is much larger than the outer-region slowness S_2.

To further test the robustness of the joint inversion algorithm, we have added 2% Gaussian noise with zero mean to the measurement data $\{g_z^*, T^*\}$ and repeated the inversion process. Figure 15 provides the recovered solution at convergence, where Figure 15 (a) displays the recovered density and Figure 15 (b) displays the recovered slowness. Since the solution is similar to the recovered solution using clean measurements as shown in Figure 13 (e) and Figure 13 (f), our inversion algorithm can tolerate reasonable noise contamination.

Shape-slowness-density recovery

In the last example we invert for the level-set function ϕ, the density contrast ρ_0 and the slowness S_1 simultaneously in the joint inversion.

We consider a salt model with the density contrast shown in Figure 2 (a) and the slowness profile shown in Figure 2 (b). The gravity data g_z^* and the traveltime data T^* are collected in the same way as that example. Similarly the computational domain $\Omega = [0, 13400]\,\mathrm{m} \times [0, 4000]\,\mathrm{m}$ is uniformly discretized into 68×21 mesh points. We initialize the level-set function to be the signed distance to an ellipse with the semi-major axis of 4000 m and the semi-minor axis of 1000 m, as shown in Figure 16 (a) and Figure 16 (b). The initial guess of the density contrast is $\rho_0 = 0.4\ \mathrm{g \cdot cm^{-3}}$, which is assumed to be a constant such that the corresponding perturbation is computed by formula (13b') in the inversion algorithm. The initial guess of the inner-region slowness is $S_1(\mathbf{r}) = 0.3\,\mathrm{s/km}$. The outer-region slowness is taken as a priori information and fixed to be $S_2(\mathbf{r}) = 0.5\,\mathrm{s/km}$ in the

inversion process. In the joint inversion the weight parameter w is computed by formula (28) after every iteration. The step size of iteration is given by formula (27) with $c_1 = 0.08$ and $c_2 = 0.5$, which leads to the recovered solution as shown in Figure 16 (c) and Figure 16 (d). In Figure 16 (c) the density contrast is recovered to be $\rho_0 \doteq 0.1972\,\mathrm{g}\cdot\mathrm{cm}^{-3}$, which is very close to the exact value $\rho_0 = 0.2\,\mathrm{g}\cdot\mathrm{cm}^{-3}$. The shape of the salt body is well imaged with a dipping flank to the left and a thin layer of horizontal extension to the right, and the varying profile of the inner-region slowness is also successfully recovered as shown in Figure 16 (d).

We have also contaminated the measurement data g_z^* and T^* by 2% Gaussian noise with zero mean and repeated the joint inversion process. The recovered solution is shown in Figure 17, where Figure 17 (a) shows the recovered density contrast and Figure 17 (b) shows the recovered slowness. Since there is no apparent distortion in the recovered solution, the inversion algorithm performs well when there is a small amount of Gaussian noise. We conclude that the level-set parametrization has successfully incorporated the structural relation into the joint inversion so that the seismic traveltime data complement the gravity data to reduce the ambiguity of inversion.

CONCLUSIONS

We have proposed a joint-inversion algorithm to invert gravity data and seismic first-arrival traveltimes simultaneously. The density contrast and slowness distributions are assumed to share common structural interfaces which are further parametrized by a level set function. We have combined the techniques of gravity inversion and seismic traveltime inversion so that the resulting joint inversion algorithm has effectively improved recovered solutions.

Synthetic examples have been provided to illustrate the effectiveness of our algorithm, including a 2-D ovoid model and the 2-D SEG/EAGE salt model. We have carried out numerical experiments for shape recovery, shape-slowness recovery and shape-slowness-density recovery, respectively. Numerical results demonstrate the flexibility of our algorithm to incorporate a priori knowledge into the inversion process. Although ideally one may invert for all model parameters simultaneously,

the solution can be unsatisfactory for complicated structures. Thus, a priori knowledge is called for to remedy the situation. The examples for the shape-slowness recovery problems illustrate advantages of various choices of a priori knowledge in different situations. Moreover, we have numerically studied the choice of the weighting parameter in the joint inversion algorithm, and Figure 6 shows that the algorithm still works well with appropriate constant values for w. Although our setup and synthetic examples are mainly for 2-D applications, the mathematical formulations are naturally extended to 3-D applications. In fact, the 3-D level-set based gravity inversion is already carried out in Lu and Qian (2015) and Li et al. (2015), and the 3-D level-set based traveltime inversion is already carried out in Li et al. (2014). Therefore, the extension of the 2-D joint-inversion algorithm to 3-D applications will not have intrinsic difficulty.

In this paper we use a single-level set formulation, which leads to a binary parameterization of the geophysical features: the subsurface is composed by two types of rock units and each unit allows a smooth heterogeneity. For complex acquisition geometries, one can consider a multiple level-set formulation to parameterize multiple rock units in the survey domain. This consists of an ongoing project.

ACKNOWLEDGMENT

Qian is supported by NSF grants 1222368 and 1522249.

REFERENCES

Afnimar, Koketsu, K., and Nakagawa, K., 2002, Joint inversion of refraction and gravity data for the three-dimensional topography of a sediment-basement interface: Geophysical Journal International, **151**, no. 1, 243–254.

Aminsadeh, F., 1996, 3-D salt and overthrust seismic models: AAPG Studies in Geology No. 42 and SEG Geophysical Developments Series No. 5.

Bain, J. E., Weyand, J., and Weber, M., Resolving complex salt features using gravity and magnetics:, AAPG Invited Lecture Series, 1991.

Birch, F., 1961, The velocity of compressional waves in rocks to 10 kilobars: Journal of Geophysical Research, **66**, no. 7, 2199–2224.

Cecil, T., Osher, S. J., and Qian, J., 2006, Simplex free adaptive tree fast sweeping and evolution methods for solving level set equations in arbitrary dimension: J. Comput. Phys., **213**, 458–473.

De Stefano, M., Golfré Andreasi, F., Re, S., Virgilio, M., and Snyder, F. F., 2011, Multiple-domain, simultaneous joint inversion of geophysical data with application to subsalt imaging: Geophysics, **76**, no. 3, R69–R80.

Eaton, D. W., Milkereit, B., and Salisbury, M. H., 2003, Hardrock seismic exploration:, number 10 SEG Books.

Fregoso, E., and Gallardo, L. A., 2009, Cross-gradients joint 3D inversion with applications to gravity and magnetic data: Geophysics, **74**, no. 4, L31–L42.

Gallardo, L. A., and Meju, M. A., 2004, Joint two-dimensional DC resistivity and seismic travel time inversion with cross-gradients constraints: Journal of Geophysical Research: Solid Earth (1978–2012), **109**, no. B3.

Gallardo, L. A., and Meju, M. A., 2007, Joint two-dimensional cross-gradient imaging of magnetotelluric and seismic traveltime data for structural and lithological classification: Geophysical Journal International, **169**, no. 3, 1261–1272.

Gallardo-Delgado, L. A., Pérez-Flores, M. A., and Gómez-Treviño, E., 2003, A versatile algorithm for joint 3D inversion of gravity and magnetic data: Geophysics, **68**, no. 3, 949–959.

Gardner, G. H. F., Gardner, L. W., and Gregory, A. R., 1974, Formation velocity and density-the diagnostic basics for stratigraphic traps: Geophysics, **39**, no. 6, 770–780.

Haber, E., and Oldenburg, D., 1997, Joint inversion: a structural approach: Inverse problems, **13**, no. 1, 63.

Hering, A., Misiek, R., Gyulai, A., Ormos, T., Dobróka, M., and Dresen, L., 1995, A joint inversion algorithm to process geoelectric and surface wave seismic data. part i: basic ideas: Geophysical Prospecting, **43**, no. 2, 135–156.

Hou, S., Solna, K., and Zhao, H., 2004, Imaging of location and geometry for extended targets using the response matrix: Journal of Computational Physics, **199**, no. 1, 317–338.

Isakov, V., Leung, S., and Qian, J., 2011, A fast local level set method for inverse gravimetry: Communications in Computational Physics, **10**, no. 4, 1044–1070.

Krahenbuhl, R. A., and Li, Y., 2006, Inversion of gravity data using a binary formulation: Geophysical Journal International, **167**, no. 2, 543–556.

Krieger, M. H., and Geisler, O., 2009, Reducing uncertainty in subsalt interpretation: A non-seismic view from integration: AAPG International Conference and Exhibition, Rio de Janeiro, Brazil, Extended Abstract, 1–9.

Lelièvre, P. G., Farquharson, C. G., and Hurich, C. A., 2012, Joint inversion of seismic traveltimes and gravity data on unstructured grids with application to mineral exploration: Geophysics, **77**, no. 1, K1–K15.

Lelièvre, P. G., Farquharson, C. G., and Bijani, R., 2015, 3D potential field inversion for wireframe surface geometry: 3D potential field inversion for wireframe surface geometry:, SEG Technical Program Expanded Abstracts 2015, 1563–1567, doi:10.1190/segam2015–5873054.1.

Leung, S., and Qian, J., 2006, An adjoint state method for three-dimensional transmission travel-time tomography using first-arrivals: Comm. Math. Sci., **4**, 249–266.

Li, W., and Leung, S., 2013, A fast local level set adjoint state method for first arrival transmission traveltime tomography with discontinuous slowness: Geophysical Journal International, **195**, no. 1, 582–596.

Li, W., Leung, S., and Qian, J., 2014, A level-set adjoint-state method for crosswell transmission-reflection traveltime tomography: Geophysical Journal International, **199**, no. 1, 348–367.

Li, W., Lu, W., and Qian, J., 2015, A multiple level set method for three-dimensional inversion of magnetic data: Submitted.

Li, W., Lu, W., and Qian, J., 2016, A level-set method for imaging salt structures using gravity data: Geophysics, **81**, no. 2, G23–G36.

Linde, N., Tryggvason, A., Peterson, J. E., and Hubbard, S. S., 2008, Joint inversion of crosshole radar and seismic traveltimes acquired at the South Oyster Bacterial Transport Site: Geophysics, **73**, no. 4, G29–G37.

Litman, A., Lesselier, D., and Santosa, F., 1998, Reconstruction of a two-dimensional binary obstacle by controlled evolution of a level-set: Inverse problems, **14**, no. 3, 685–706.

Lu, W., and Qian, J., 2015, A local level set method for three-dimensional inversion of gravity gradient data: Geophysics, **80**, no. 1, G35–G51.

Lu, W., Leung, S., and Qian, J., 2015, An improved fast local level set method for three-dimensional inverse gravimetry: Inverse Problems and Imaging, **9**, no. 2, 479–509.

Moorkamp, M., Heincke, B., Jegen, M., Roberts, A. W., and Hobbs, R. W., 2011, A framework for 3-D joint inversion of MT, gravity and seismic refraction data: Geophysical Journal International, **184**, no. 1, 477–493.

Nielsen, L., and Jacobsen, B. H., 2000, Integrated gravity and wide-angle seismic inversion for two-dimensional crustal modelling: Geophysical Journal International, **140**, no. 1, 222–232.

Osher, S. J., and Santosa, F., 2001, Level set methods for optimization problems involving geometry and constraints I. Frequencies of a two-density inhomogeneous drum: J. Comput. Phys., **171**, no. 1, 272–288.

Osher, S. J., and Sethian, J. A., 1988, Fronts propagating with curvature dependent speed: algorithms based on Hamilton-Jacobi formulations: J. Comput. Phys., **79**, no. 1, 12–49.

Papadopoulos, D., Herty, M., Rath, V., and Behr, M., 2011, Identification of uncertainties in the shape of geophysical objects with level sets and the adjoint method: Computational Geosciences, **15**, no. 4, 737–753.

Qian, J., and Symes, W. W., 2002, An adaptive finite difference method for traveltime and amplitude: Geophysics, **67**, 167–176.

Rudin, L., Osher, S. J., and Fatemi, E., 1992, Nonlinear total variation based noise removal algorithms: Physica D, **60**, 259–268.

Santosa, F., 1996, A level-set approach for inverse problems involving obstacles: Control, Optimizat. Calculus Variat., **1**, 17–33.

Savino, J. M., Rodi, W. L., and Masso, J. F., Inversion modeling of multiple geophysical data sets for geothermal exploration: application to roosevelt hot springs area. final report:, Technical report, S-Cubed, La Jolla, CA (USA), 1982.

Sussman, M., Smereka, P., and Osher, S. J., 1994, A level set approach for computing solutions to incompressible two-phase flows: J. Comput. Phys., **114**, no. 1, 146–159.

Tartaras, E., Masnaghetti, L., Lovatini, A., Hallinan, S., Mantovani, M., Virgilio, M., Soyer, W., Stefano, M., Snyder, F., Subia, J., and Dugoujard, T., 2011, Multi-property earth model building through integration of seismic, EM and potential field data with other G&G data: case studies from complex exploration areas: 12th International Congress of the Brazilian Geophysical Society & EXPOGEF, SEG Global Meeting Abstracts.

van den Doel, K., Ascher, U., and Leitao, A., 2010, Multiple level sets for piecewise constant surface reconstruction in highly ill-posed problems: J. Sci. Comput., **43**, 44–66.

Zhao, H. K., Chan, T., Merriman, B., and Osher, S., 1996, A variational level set approach to multiphase motion: J. Comput. Phys., **127**, no. 1, 179–195.

Zhao, H. K., 2005, A fast sweeping method for eikonal equations: Mathematics of computation, **74**, no. 250, 603–627.

Zheglova, P., Farquharson, C. G., and Hurich, C. A., 2013, 2-D reconstruction of boundaries with level set inversion of traveltimes: Geophysical Journal International, **192**, no. 2, 688–698.

LIST OF FIGURES

7 Shape-slowness recovery for a 2-D salt model with varying inner-region slowness. The exact structure and the setup of data acquisition are shown in Figure 2. In this example the density contrast ρ_0 and the outer-region slowness S_2 are taken as a priori information. (a) Initial guess of density. (b) Initial guess of slowness. (c) Recovered density by gravity inversion. (d) Recovered slowness by traveltime inversion. (e) Recovered density by joint inversion. (f) Recovered slowness by joint inversion. In (c)-(f) the line contour illustrates the exact salt interface.

8 Shape-slowness recovery for a 2-D salt model with varying inner-region slowness. 2% Gaussian noises are added to the measurements. The density contrast ρ_0 and the outer-region slowness S_2 are taken as a priori information. (a) Recovered density by joint inversion. (b) Recovered slowness by joint inversion. The line contour illustrates the exact salt interface.

9 Shape-slowness recovery for the 2-D SEG/EAGE salt model. The slowness is extracted from the original 3-D SEG/EAGE salt model; the density contrast between salt and its sediment is linearly decreasing with the depth. The gravity data g_z^* and the first-arrival traveltimes T^* are collected in the same way as the previous example. (a) Exact density. (b) Exact slowness.

10 Shape-slowness recovery for the 2-D SEG/EAGE salt model. The inner-region slowness S_1 and density contrast ρ_0 are taken as a priori information. (a) Initial guess of density. (b) Initial guess of slowness. (c) Recovered density by gravity inversion. (d) Recovered slowness by traveltime inversion. (e) Recovered density by joint inversion. (f) Recovered slowness by joint inversion. In (c)-(f) the line contour illustrates the exact salt interface.

11 Shape-slowness recovery for the 2-D SEG/EAGE salt model. 2% Gaussian noises are added to the measurements. The inner-region slowness S_1 and density contrast ρ_0 are taken as a priori information. (a) Recovered density by joint inversion. (b) Recovered slowness by joint inversion.

12 Shape-slowness recovery for a 2-D ovoid model. (a) Exact density. (b) Exact slowness. The gravity data g_z^* are collected at a 700 m survey line $\Gamma_g = [-300, 400]\,\mathrm{m} \times \{z = -10\}\,\mathrm{m}$, and there are 71 observation points uniformly distributed on Γ_g. The first-arrival traveltimes are measured on the mesh grids along three sides of the boundary; there are 20 point sources distributed on two sides of

the survey domain: $\mathbf{r}_{\mathbf{s}}^{j} = (-290,\, 10*(2j-1))\,\mathrm{m}$ with $j = 1, 2, \cdots, 10$ and $\mathbf{r}_{\mathbf{s}}^{j} = (390,\, 20*(j-10))\,\mathrm{m}$ with $j = 11, 12, \cdots, 20$. In (b) the asterisks illustrate the locations of seismic sources and the circles label the locations of receivers.

13 Shape-slowness recovery for a 2-D ovoid model. The density contrast ρ_0 is taken as a priori information. (a) Initial guess of density. (b) Initial guess of slowness. (c) Recovered density by gravity inversion. (d) Recovered slowness by traveltime inversion. (e) Recovered density by joint inversion. (f) Recovered slowness by joint inversion. In (c)-(f) the line contour illustrates the exact structure.

14 Shape-slowness recovery for a 2-D ovoid model; cross-sections of slowness in the joint inversion. The density contrast ρ_0 is taken as a priori information. (a) Cross-section of slowness along $x = 100\,\mathrm{m}$. (b) Cross-section of slowness along $z = 100\,\mathrm{m}$.

15 Shape-slowness recovery for a 2-D ovoid model. 2% Gaussian noises are added to the measurements. The density contrast ρ_0 is taken as a priori information. (a) Recovered density by joint inversion. (b) Recovered slowness by joint inversion. The line contour illustrates the exact structure.

16 Shape-slowness-density recovery for a 2-D salt model with varying inner-region slowness. The exact structure and the setup of data acquisition are shown in Figure 2. The outer-region slowness S_2 is taken as a priori information. (a) Initial guess of density. (b) Initial guess of slowness. (c) Recovered density by joint inversion, the recovered density $\rho_0 \doteq 0.1972$. (d) Recovered slowness by joint inversion.

17 Shape-slowness-density recovery for a 2-D salt model with varying inner-region slowness. 2% Gaussian noises are added to the measurements. The outer-region slowness S_2 is taken as a priori information. (a) Recovered density by joint inversion, the recovered density $\rho_0 \doteq 0.1944$. (b) Recovered slowness by joint inversion.

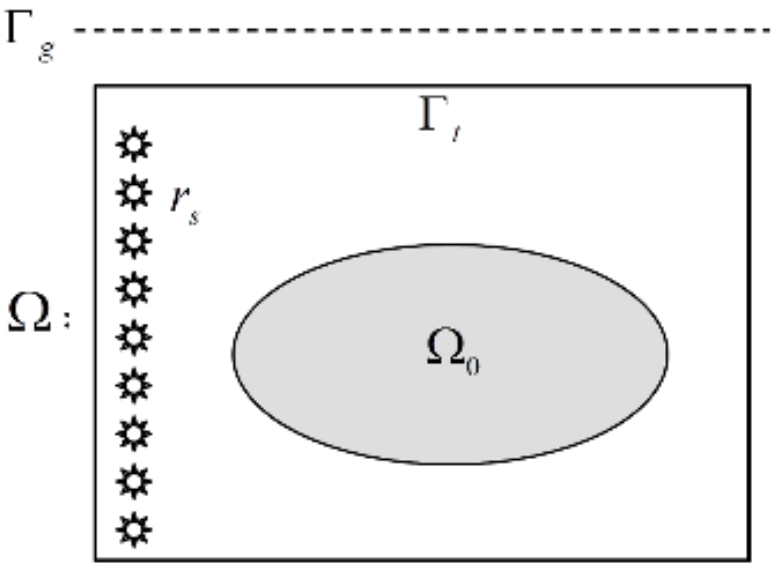

Figure 1: An illustration of the problem setup.

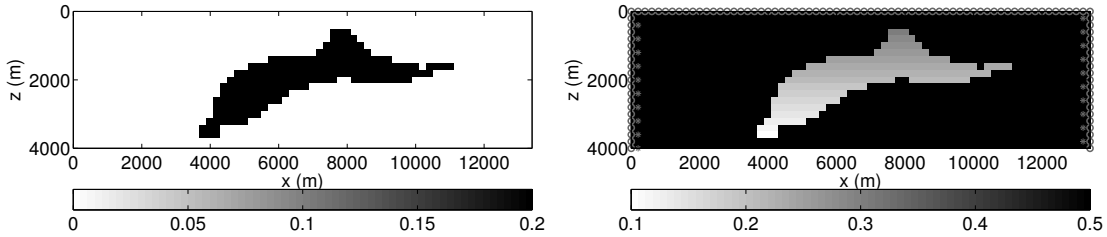

Figure 2: A 2-D salt model with varying inner-region slowness. This model is studied in the problems of shape recovery, shape-slowness recovery, and shape-slowness-density recovery. (a) Exact density. (b) Exact slowness. The gravity data g_z^* are collected along a 40 km survey line $\Gamma_g = [-13000, 27000]\,\mathrm{m} \times \{z = -100\}\,\mathrm{m}$, and there are 41 observation points uniformly distributed on Γ_g. The first-arrival traveltimes T^* are measured at the mesh points located on three sides of the boundary, and there are 20 point sources located on two sides of the domain: $\mathbf{r}_\mathbf{s}^j = (200,\, 200 * (2j-1))\,\mathrm{m}$ with $j = 1, 2, \cdots, 10$ and $\mathbf{r}_\mathbf{s}^j = (13200,\, 400 * (j-10))\,\mathrm{m}$ with $j = 11, 12, \cdots, 20$; in (b) the asterisks illustrate the sources and the circles display the receivers.

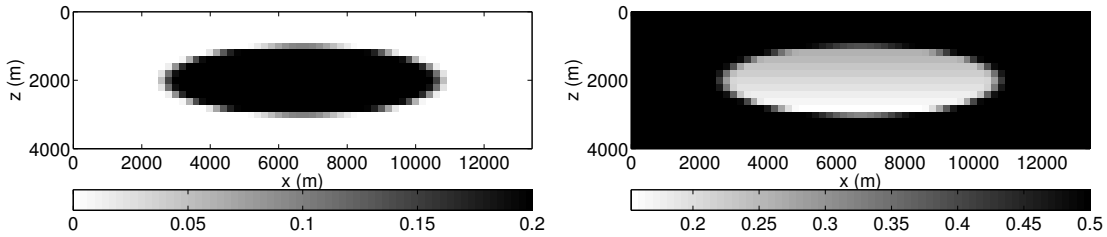

Figure 3: Shape recovery for a 2-D salt model with varying inner-region slowness. (a) Initial density. (b) Initial slowness.

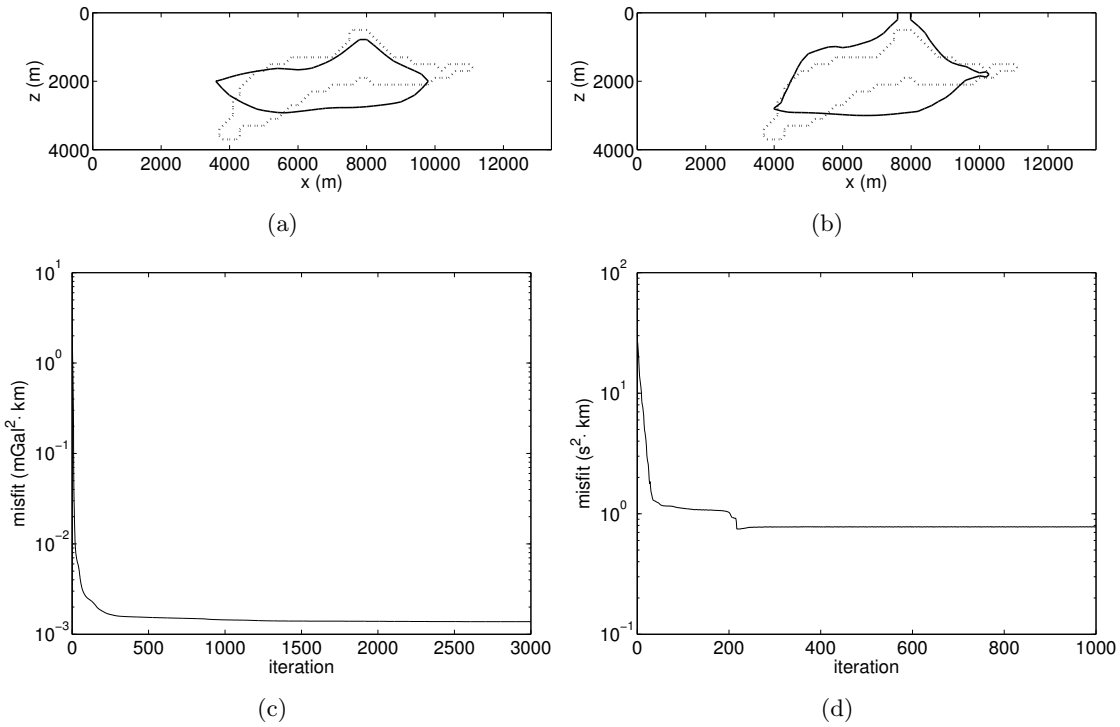

Figure 4: Shape recovery for a 2-D salt model with varying inner-region slowness. Recovered solutions from gravity inversion and traveltime inversion. (a) Result by gravity inversion, $C = 1303$. (b) Result by traveltime inversion, $C = 1300$. In (a) and (b), the solid line plots the recovered interface and the dashed line displays the exact structure; the value of C equals the number of mesh grids with correct lithology in the recovered solution. (c) Convergence history of gravity inversion. (d) Convergence history of traveltime inversion.

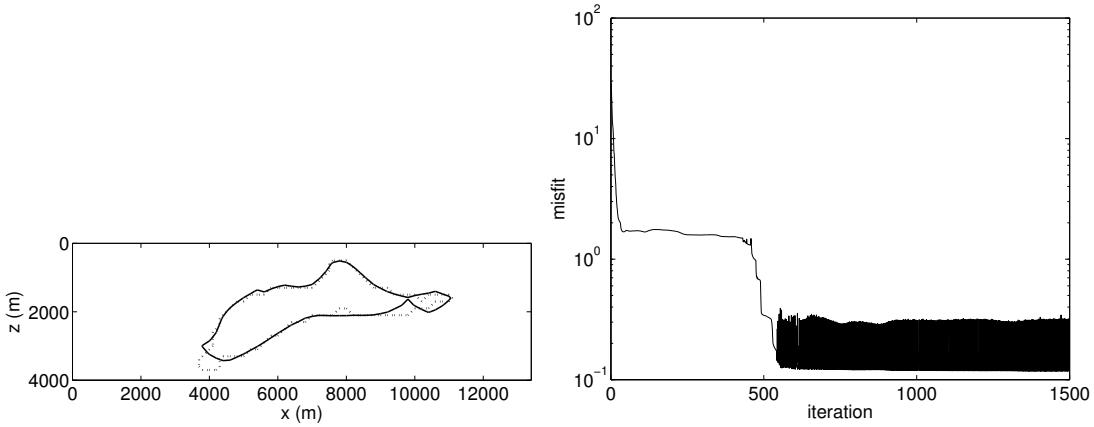

(a) (b)

Figure 5: Shape recovery for a 2-D salt model with varying inner-region slowness. Results using joint inversion. (a) Result by joint inversion, $C = 1403$. The solid line plots the recovered interface and the dashed line displays the exact structure; the value of C equals the number of mesh grids with correct lithology in the recovered solution. (b) Convergence history of joint inversion.

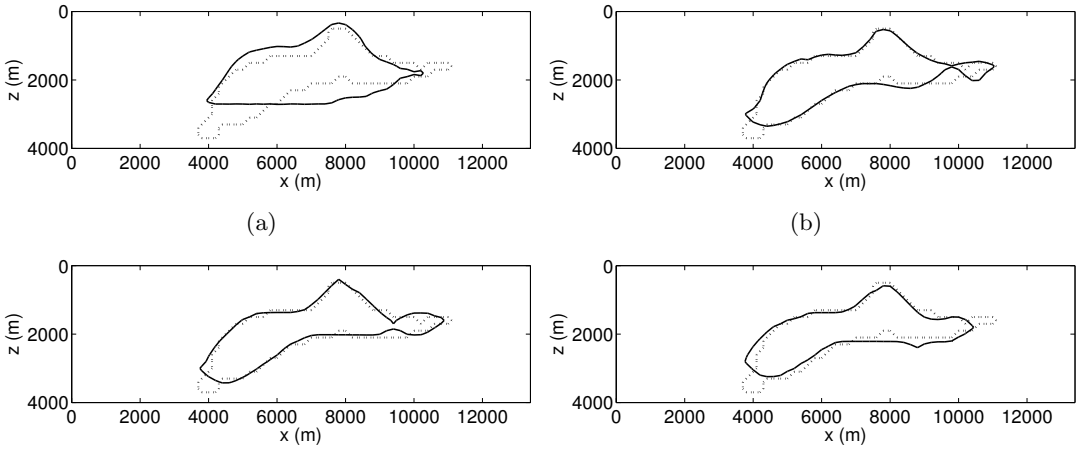

Figure 6: Shape recovery for a 2-D salt model with varying inner-region slowness. Results of joint inversion with various weight parameters. The solid line plots the recovered interface and the dashed line displays the exact structure. w is the weight parameter in formula (11), and C denotes the number of mesh grids with correct lithology in the recovered solution. (a) $w = 0.1$, $C = 1325$. (b) $w = 1$, $C = 1398$. (c) $w = 10$, $C = 1390$. (d) $w = 100$, $C = 1376$.

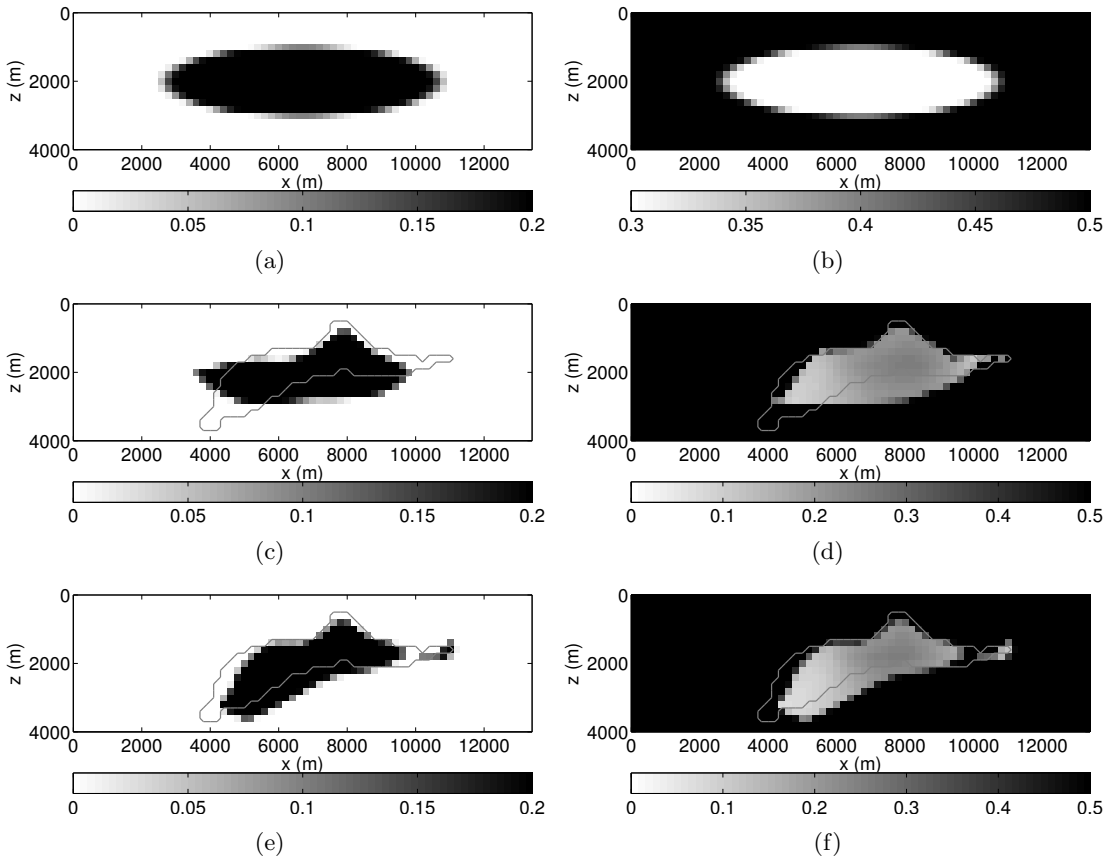

Figure 7: Shape-slowness recovery for a 2-D salt model with varying inner-region slowness. The exact structure and the setup of data acquisition are shown in Figure 2. In this example the density contrast ρ_0 and the outer-region slowness S_2 are taken as a priori information. (a) Initial guess of density. (b) Initial guess of slowness. (c) Recovered density by gravity inversion. (d) Recovered slowness by traveltime inversion. (e) Recovered density by joint inversion. (f) Recovered slowness by joint inversion. In (c)-(f) the line contour illustrates the exact salt interface.

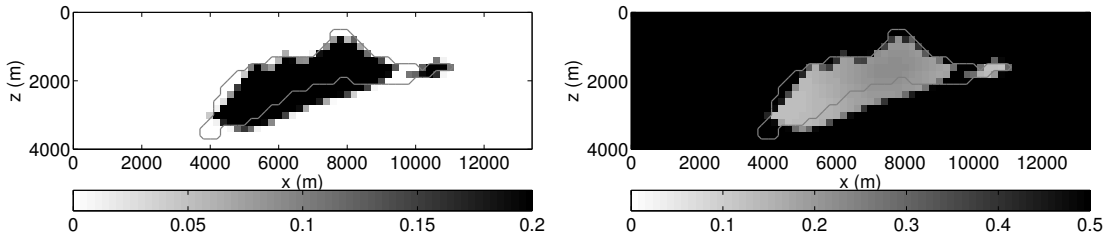

Figure 8: Shape-slowness recovery for a 2-D salt model with varying inner-region slowness. 2% Gaussian noises are added to the measurements. The density contrast ρ_0 and the outer-region slowness S_2 are taken as a priori information. (a) Recovered density by joint inversion. (b) Recovered slowness by joint inversion. The line contour illustrates the exact salt interface.

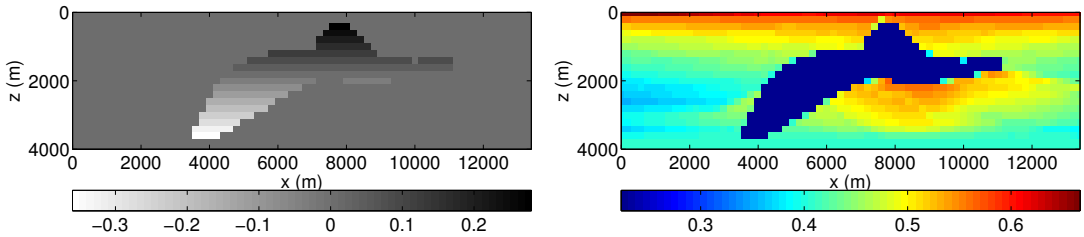

(a) (b)

Figure 9: Shape-slowness recovery for the 2-D SEG/EAGE salt model. The slowness is extracted from the original 3-D SEG/EAGE salt model; the density contrast between salt and its sediment is linearly decreasing with the depth. The gravity data g_z^* and the first-arrival traveltimes T^* are collected in the same way as the previous example. (a) Exact density. (b) Exact slowness.

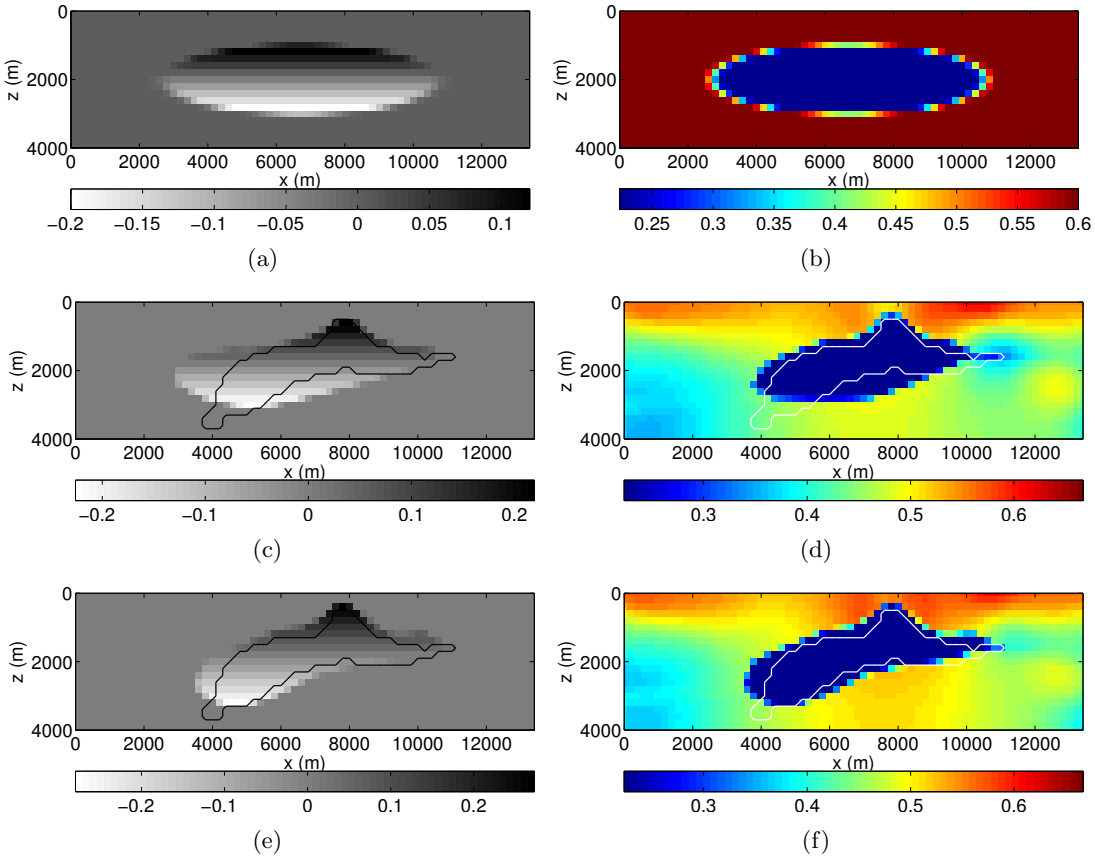

Figure 10: Shape-slowness recovery for the 2-D SEG/EAGE salt model. The inner-region slowness S_1 and density contrast ρ_0 are taken as a priori information. (a) Initial guess of density. (b) Initial guess of slowness. (c) Recovered density by gravity inversion. (d) Recovered slowness by traveltime inversion. (e) Recovered density by joint inversion. (f) Recovered slowness by joint inversion. In (c)-(f) the line contour illustrates the exact salt interface.

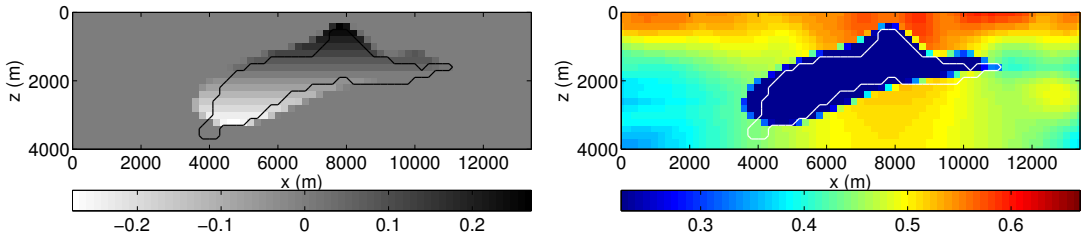

Figure 11: Shape-slowness recovery for the 2-D SEG/EAGE salt model. 2% Gaussian noises are added to the measurements. The inner-region slowness S_1 and density contrast ρ_0 are taken as a priori information. (a) Recovered density by joint inversion. (b) Recovered slowness by joint inversion.

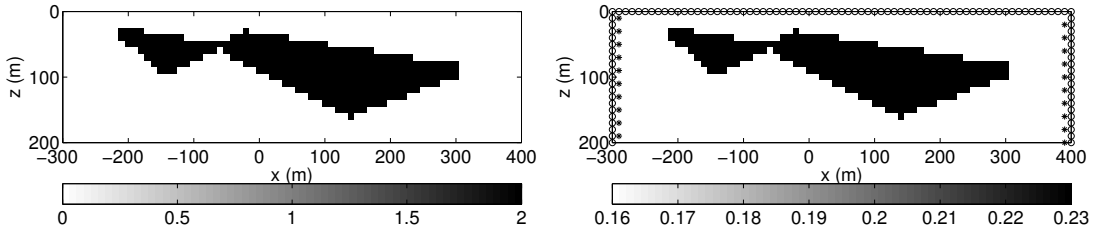

Figure 12: Shape-slowness recovery for a 2-D ovoid model. (a) Exact density. (b) Exact slowness. The gravity data g_z^* are collected at a 700 m survey line $\Gamma_g = [-300, 400]\,\mathrm{m} \times \{z = -10\}\,\mathrm{m}$, and there are 71 observation points uniformly distributed on Γ_g. The first-arrival traveltimes are measured on the mesh grids along three sides of the boundary; there are 20 point sources distributed on two sides of the survey domain: $\mathbf{r}_\mathbf{s}^j = (-290,\, 10 * (2j-1))\,\mathrm{m}$ with $j = 1, 2, \cdots, 10$ and $\mathbf{r}_\mathbf{s}^j = (390,\, 20 * (j-10))\,\mathrm{m}$ with $j = 11, 12, \cdots, 20$. In (b) the asterisks illustrate the locations of seismic sources and the circles label the locations of receivers.

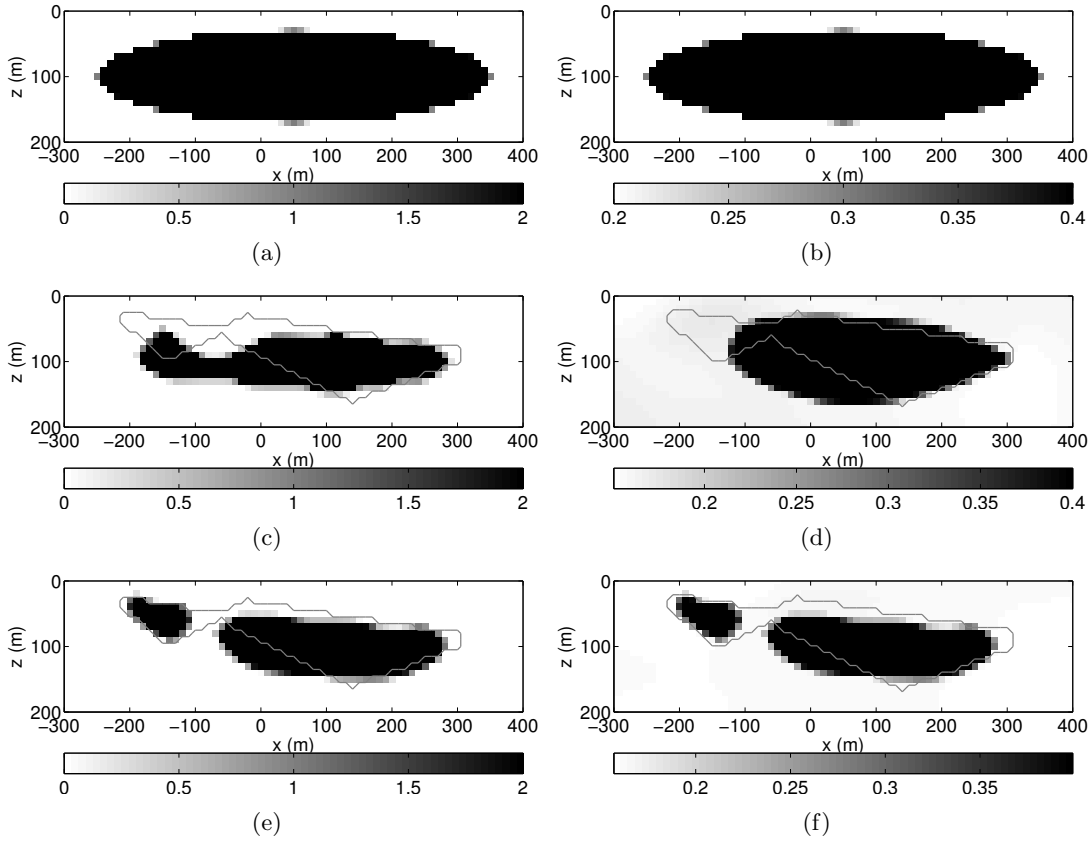

Figure 13: Shape-slowness recovery for a 2-D ovoid model. The density contrast ρ_0 is taken as a priori information. (a) Initial guess of density. (b) Initial guess of slowness. (c) Recovered density by gravity inversion. (d) Recovered slowness by traveltime inversion. (e) Recovered density by joint inversion. (f) Recovered slowness by joint inversion. In (c)-(f) the line contour illustrates the exact structure.

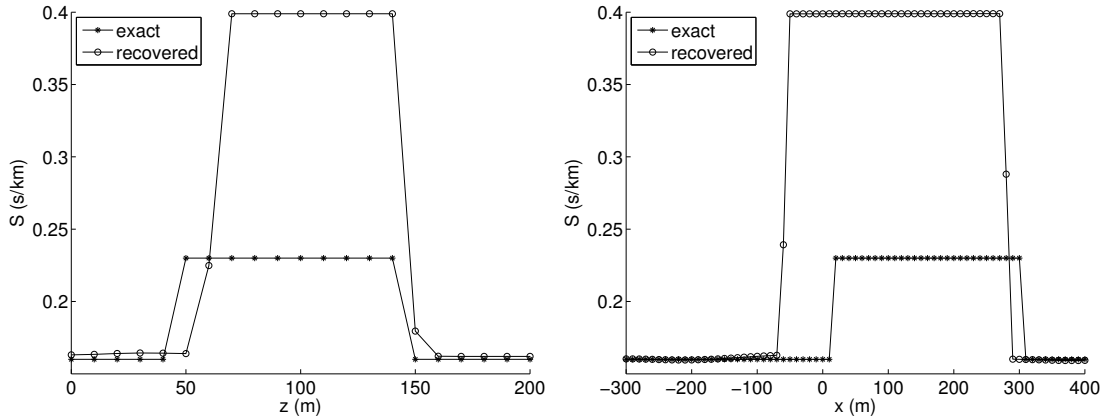

(a) (b)

Figure 14: Shape-slowness recovery for a 2-D ovoid model; cross-sections of slowness in the joint inversion. The density contrast ρ_0 is taken as a priori information. (a) Cross-section of slowness along $x = 100\,\mathrm{m}$. (b) Cross-section of slowness along $z = 100\,\mathrm{m}$.

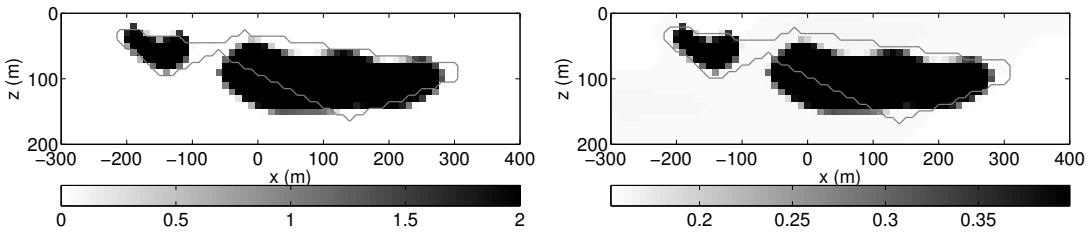

(a) (b)

Figure 15: Shape-slowness recovery for a 2-D ovoid model. 2% Gaussian noises are added to the measurements. The density contrast ρ_0 is taken as a priori information. (a) Recovered density by joint inversion. (b) Recovered slowness by joint inversion. The line contour illustrates the exact structure.

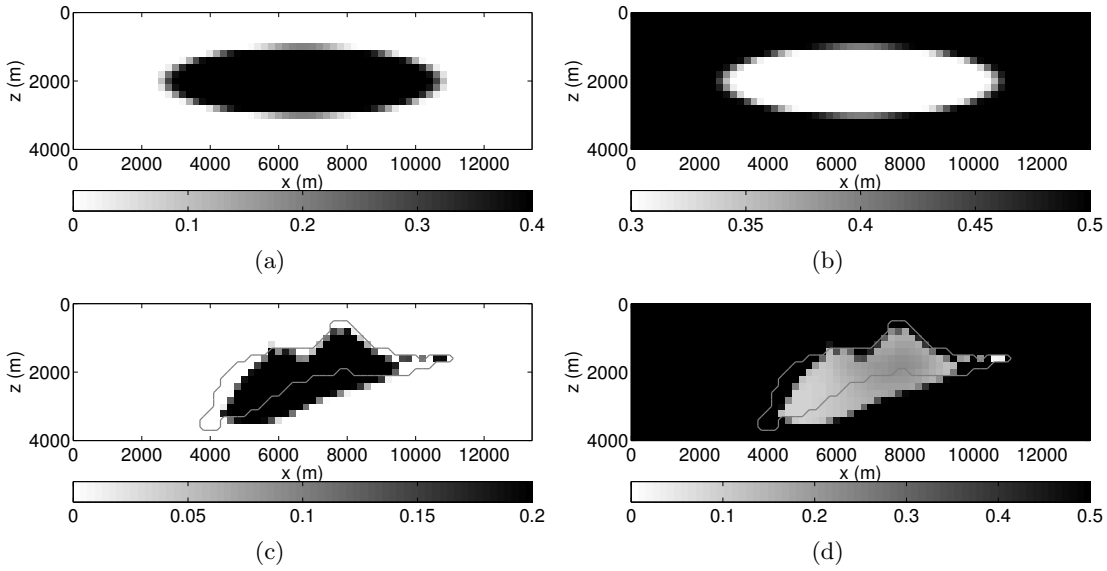

Figure 16: Shape-slowness-density recovery for a 2-D salt model with varying inner-region slowness. The exact structure and the setup of data acquisition are shown in Figure 2. The outer-region slowness S_2 is taken as a priori information. (a) Initial guess of density. (b) Initial guess of slowness. (c) Recovered density by joint inversion, the recovered density $\rho_0 \doteq 0.1972$. (d) Recovered slowness by joint inversion.

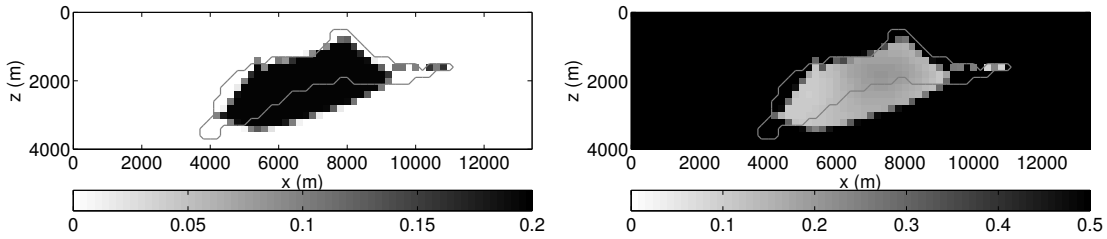

Figure 17: Shape-slowness-density recovery for a 2-D salt model with varying inner-region slowness. 2% Gaussian noises are added to the measurements. The outer-region slowness S_2 is taken as a priori information. (a) Recovered density by joint inversion, the recovered density $\rho_0 \doteq 0.1944$. (b) Recovered slowness by joint inversion.